A Solid Immersion Interference Lithography System for Imaging Ultra-High Numerical Apertures with High-Aspect Ratios in Photoresist using Resonant Enhancement from Effective Gain Media

Prateek Mehrotra[1,**], Chris A. Mack[2], Richard J. Blaikie[1,*]

[1]The MacDiarmid Institute for Advanced Materials and Nanotechnology,
Department of Electrical and Computer Engineering, University of Canterbury, Christchurch, New Zealand
[2]Department of Chemical Engineering, The University of Texas at Austin, Austin, TX
*Current Address: Department of Physics, University of Otago, PO Box 56, Dunedin, New Zealand

ABSTRACT

In the last year our Solid Immersion Lloyd's Mirror Interference Lithography (SILMIL) system has proved to be a successful tool for evanescent interferometric lithography (EIL). The initial goal was to use SILMIL in conjunction with the surface plasmon polariton (SPP) surface states at the resist-metal interface. Through this resonance, we aimed to counter the decay of evanescent images created using EIL. By analyzing the theory in greater detail we were able to develop a better understanding of the resonance phenomena. In this paper, details of the design of SILMIL and how one may utilize it to produce ultra-high numerical apertures (NAs) are given, as well as an introduction to the resonance phenomena and the mechanism behind it. We introduce a new method that requires a gain medium (one that has a negative loss) to achieve significant enhancements, and present an effective gain medium by using a high-index dielectric on low-index media. We present results at $\lambda = 405$ nm using such an effective gain medium and also provide a feasible design example at the lithography standard $\lambda = 193$ nm.

Keywords: Evanescent interference lithography, solid-immersion interference lithography, reflection resonance, effective gain medium, ultra-high numerical aperture, high aspect ratio

1. INTRODUCTION

The semiconductor industry has historically reduced the feature sizes used in integrated circuits by a factor of 2 every 4 to 6 years. For this reason, advances in super-resolution optical imaging are being aggressively pursued for applications in imaging, data storage and lithography. While the general trend in the semiconductor industry has been to reduce the wavelength and increase the numerical aperture (NA) of the system, the industry is now looking for alternative means to achieve higher resolutions. At present much of the semiconductor industry operates at $\lambda = 193$ nm and uses water as an immersion fluid, thus allowing a maximum system NA of 1.35. Many manufacturers also employ successive interference-like lithography steps and use double patterning to increase the packing density. Higher index immersion liquids and lens materials, while enabling higher NAs, are not yet available and will require much research and development before they are.

** *pratro@gmail.com*

Extreme Ultra-violet (EUV) systems operating at λ = 13.5 nm are extensively pursued, but are expensive to run, offer a lower throughput than present systems, require greater maintenance and require high vacuums and reflective lensing due to the high absorption of most materials available at that wavelength. Their future availability is still in doubt.

Other optical techniques are also being pursued that aim to pattern by beating the diffraction limit as opposed to reducing the wavelength and increase the *NA*. One such technique is Absorbance Modulation Optical Lithography (AMOL),[1-7] which has attracted considerable attention. It is an innovative optical technique that is in many ways a lithographic analogue of Stimulated Emission Depletion (STED) Microscopy.[8-9] AMOL uses two wavelengths of light each of which change the refractive index and extinction coefficient of a special absorbance modulation layer depending on the intensity ratio of the two wavelengths. The competing wavelengths thus allow imaging of a sub-diffraction feature. Plasmonics has also been looked to for solutions to beating the diffraction limit ever since the classical paper by Sir John Pendry[10] was published and the superlens was experimentally demonstrated by two groups independently; Fang *et al*.[11] and Melville & Blaikie.[12]

Alternative non-optical techniques are also being pursued, *e.g*., there is a considerable amount of literature available for the massively parallel electron beam lithography tool called MAPPER which is being developed to allow higher resolutions and a higher throughput.[13-18] Similarly, the directed self-assembly of block copolymers for nano-lithography has also garnished considerable research attention from universities and industry.[19-23]

In this paper we talk about a well-known optical interference lithography technique that is of interest to researchers known as solid-immersion interference lithography. This allows interference of two evanescent waves at the opposite ends of the full *NA* to create an ultra-high *NA* image[24-26] offering the resolutions that the industry is interested in achieving. However at *NA*s beyond the refractive index of the photoresist (~1.7), the image is evanescent, resulting in a pattern that is confined only to the surface of the photoresist. This makes pattern transfer very difficult and renders the technique of little practical use to the industry. We show that there is a simple way to get around this physical limit which makes this technique feasible and of great potential interest to the lithographic community.

2. EXPERIMENTAL CONDITIONS FOR SOLID IMMERSION LLOYD'S MIRROR INTERFERENCE LITHOGRAPHY (SILMIL)

In SILMIL[27], a Lloyd's mirror embedded inside a prism is used to perform interferometric lithography, thus allowing the system to achieve a smaller half-pitch than may be achieved without the prism. Figure 1 shows how this is achieved. The incident beam is interfered with a reflection of itself to create an interference pattern in an imaging stack. Index matching liquid, photoresist and the substrate (silicon) make up the important layers in the imaging stack for traditional EIL, and this stack is pressed into contact with the bottom of the prism. The simple prism geometry (cube) allows most spurious reflections (red dashed) to be driven out of the system[1] reducing the amount of noise that is added to the imaging stack. This and other practical design and implementation issues have been resolved to allow for repeatable experiments to be performed with this system, as described in the following sub-sections.

2.1 Laser & Spatial Filtering

At λ = 405 nm a Ondax[28] SureLock[TM] wavelength-stabilized single mode, single frequency laser with a 40mW output and coherence length > 1 meter was used. A coherence length of at least several centimeters is essential for the proper operation of SILMIL. A spatial filter arrangement is used by focusing the laser output and filtering with a 5 μm pinhole, resulting in an approximately Gaussian single-mode beam profile. For conventional Lloyd's mirror interferometric lithography, plane waves could be used by employing beam-shaping and collimating optics. While this would be ideal,

we did not use this method here. Instead we directly collimated the output of the pinhole to the required spot size using a lens. This method allows a higher intensity beam and hence a shorter exposure time, which is advantageous. The reasons for this are discussed later in section 2.4. Collimation is achieved by mounting the collimating lens on a kinematic mirror mount and attaching to a switchable magnetic base. This bypasses any optical axis misalignments that exist between the pinhole and the pinhole mount and allows for sufficient degrees of freedom for proper collimation. Proper collimation is achieved by adjusting the various degrees of freedom to allow a spatial filter output with a cylindrically symmetric intensity variation.
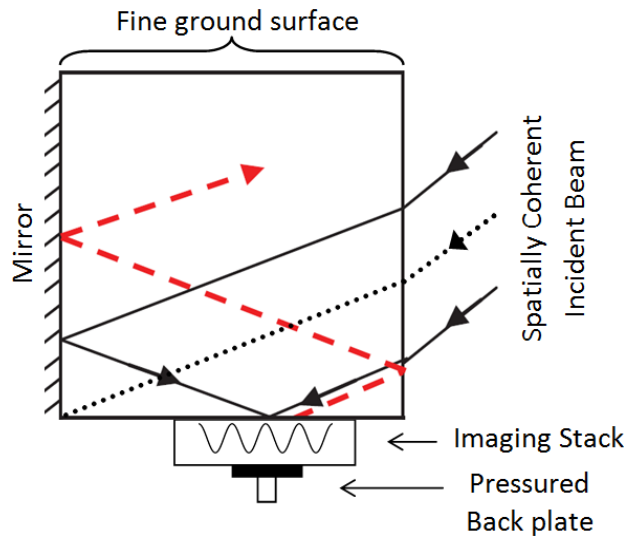

Figure 1. Plan view of SILMIL basic operation, showing incident plane wave (black solid arrows) and spurious reflections (red dashed arrow).

2.2 Prism Setup & Alignment

For our wavelength of 405 nm we used a cube-shaped Yttrium Aluminum Garnet (YAG) prism with a refractive index of ~1.856. The prism is held in a custom designed cage as depicted in Fig. 2.
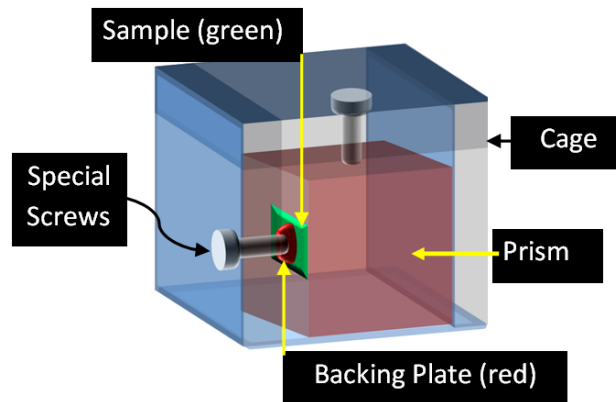

Figure 2. Prism and cage arrangement with backing plate, screws and sample for SILMIL.

Figure 3 illustrates a simplified setup in which the solid blue arrows show the path of the collimated beam towards the prism and the dashed blue arrows show the return path of the beam after it has been internally reflected by the prism. Also shown are the available degrees of freedom.
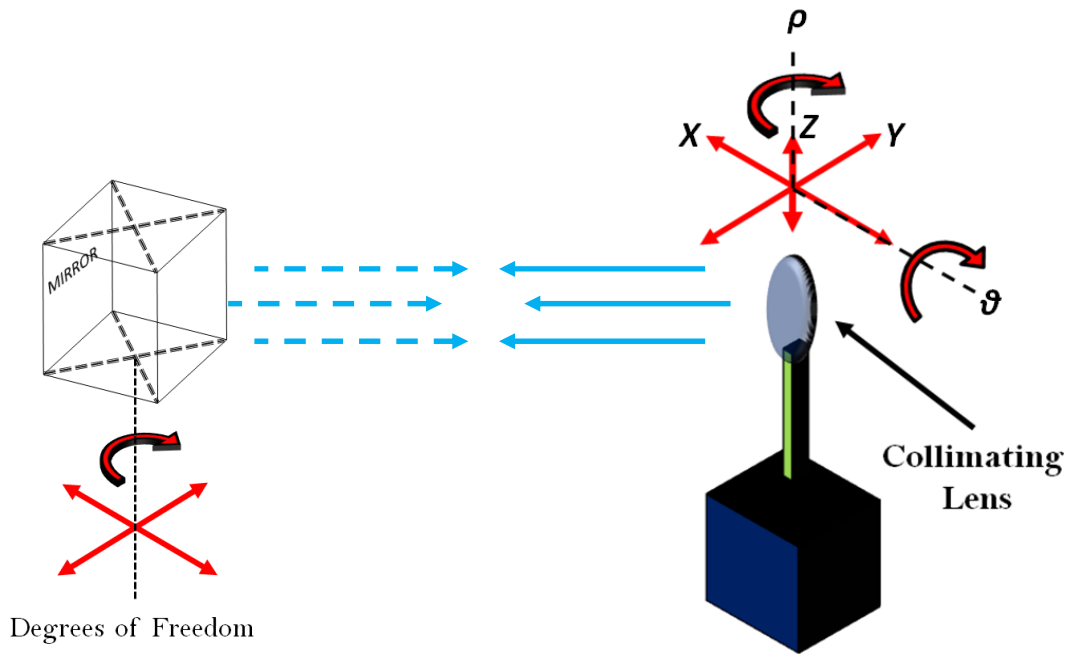

Figure 3. Proper prism alignment with the incident beam (solid arrows) is achieved by observing the reflected beam (shown as the dashed arrows).

The goal is to adjust the prism in both the *X* and *Y* axes so that center of the collimated spot (as shown by the dotted line in Fig. 1) hits the interface between the mirror and sample side on the inside of the prism splitting the collimated beam in to two equal portions. To achieve this, we observe the reflection of the collimated spot from the prism. Adjustment is easier when the collimating lens is deliberately shifted a slight amount in the direction normal to the lens so that the spot size reduces in diameter with increasing distance from the lens. When the prism is adjusted correctly, the reflection should be two diverging semi-circular spots. Figure 4 (a) indicates the intentional misalignment of the lens to achieve a decreasing spot size. Figure 4 (b) illustrates what the back reflection from the prism in the opposite direction should look like when prism alignment is complete. The collimating lens should be moved back to the correct position following the prism alignment.
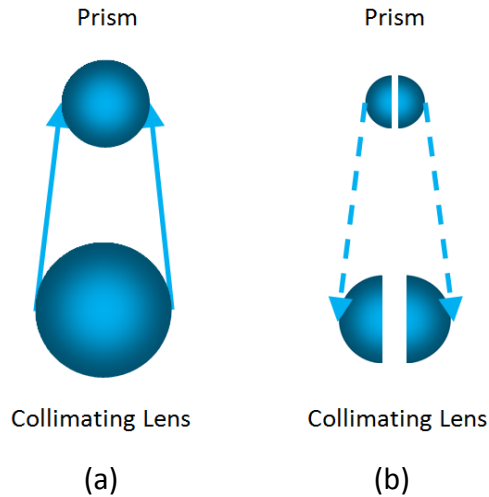
Figure 4. The prism is aligned by first moving the lens off the optical axis and achieving a decreasing spot size as (a) the beam travels towards the prism, then (b) aligning the prism such that the reflected spot is split in two equal parts.

Setting the prism orientation to achieve the desired *NA* is the next objective. The refractive index of undoped Yttrium Aluminum Garnet prism at $\lambda = 405$ nm is measured and reported to be ~1.856.[29] This allows us to calculate the expected *NA* when the prism is rotated to a particular angle. At an angle of 20° as depicted in Fig. 5, we expect a *NA* of 1.824, which is the *NA* used for all the experiments reported here. Under these conditions the interference pattern in the resist has a 55-nm half pitch, and the exposure in the resist is dominated by evanescent fields.
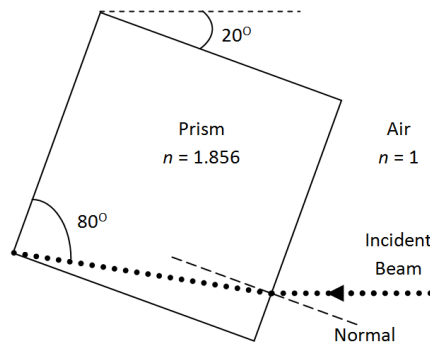

Figure 5. Yttrium Aluminum Garnet prism rotation required for *NA* = 1.824 at $\lambda = 405$ nm,

2.3 Imaging Stack Preparation

The imaging stack consists of various layers of materials stacked together to transfer the evanescent interferometric field profile into the photoresist. The stack is made up of a 400 nm layer of photoresist spun on a silicon wafer, with ~15nm of poly-vinyl alcohol (PVA) spun on the photoresist. Finally, a few drops of index matching liquid (IML) are placed on the PVA layer. The purpose of the PVA layer is to prevent the IML from attacking the photoresist. Table 1 details the optical properties of various materials, some of which are used in the stack later. The IML is not a constant thickness thin film and while we would like it to wet the surface of the three layers stack uniformly, effects such as difference in surface energies come into the picture. The stack is brought into contact with the prism and locked in place reasonably tightly inside the cage using the backing plate so that the evanescent image does not fully decay within the IML layer.

Table 1. Optical properties of several materials discussed in this paper

Optical properties of various media			
Material	**Refractive Index/Optical Property**	**Thickness**	**Reference**
Yttrium Aluminum Garnet prism	$n = 1.856$ @ $\lambda = 405$ nm	Cubic prism	[29]
Index Matching Liquid (Cargille High Index Liquid – Series B with $n = 1.7$ @ $\lambda = 589.3$ nm)	$n = 1.7714$ @ $\lambda = 404.7$ nm	Few drops, then pressed between stack and prism	[30]
Poly-vinyl Alcohol	$n \sim 1.5$ @ $\lambda = 405$ nm	12-15 nm	[31]
Photoresist	**AZ HiR 1075** – $n = 1.682+0.031i$ @ $\lambda = 405$ nm **Industry standard** $n = 1.7 + 0.02i$ @ $\lambda = 193$ nm	Varies with wavelength & *NA*	[32]
Silicon	$n = 5.42 + 0.329i$ @ $\lambda = 405$ nm	Assume Semi-infinite	[33]
Silicon Dioxide (Fused Quartz)	$n = 1.47$ @ $\lambda = 405$ nm	Varies with wavelength & *NA*	[33]
Hafnium Oxide (HfO) (RF target)	$n \sim 2$ *(varies)* @ $\lambda = 405$ nm	Varies with wavelength & *NA*	Measured with Attenuated Total Reflectance
Aluminum Oxide	$n \sim 2.08$ (*varies*) (thin film on polished fused silica) @ $\lambda = 193$ nm $n \sim 1.92$ (Sapphire prism) @ $\lambda = 193$ nm	Thin film thickness varies with wavelength & *NA*	[25, 34]

2.4 Exposure Dosage & Results

A pseudo-dosage (or pseudo-dose) was used to characterize and compare the evanescent interferometric lithography experiments. For a particular *NA*, the pseudo-dose is simply the reading on the power meter at the center of the collimated spot, multiplied by the time taken for the exposure in minutes. This allowed a very simple relation to be established between the exposure dosage and pattern quality and depth.

After exposure, the sample is removed from the cage and washed in toluene for 15 seconds, dried with compressed nitrogen and then rinsed in DI water. These two steps remove the IML and PVA respectively. The sample is then developed for 1 minute in 1.59% solution of tetra-methyl ammonium hydroxide (AZ326 MIF developer diluted 2:1 with deionized water, AZ Electronic Materials).[32] Finally, the sample is dried with compressed nitrogen once again before being imaged by an Atomic Force Microscope (AFM).

We found two advantages to having a shorter exposure time: it allows faster exposures and quicker data accumulation, and also mitigates additive noise that would otherwise be present in the final image. Figure 6 illustrates atomic-force microscope (AFM) scans of resist images exposed using various pseudo-doses for constant collimated beam intensity, with data extracted from these images summarized in Fig. 7. Pattern depth is defined as the difference in height between the peak and trough of the resist modulation with respect to the silicon substrate. As expected, a higher dose creates deeper features, but also reduces pattern quality through background exposure (DC component) that acts to reduce

image contrast. However, our results show that in addition to expected background exposure, the samples with longer exposure times also exhibit undesirable 'bumps' throughout the image plane visible as an irregular color variation. We believe this is a result of intensity variation due to interference from thickness variations in the index matching liquid (IML) as the IML is not a constant thickness thin film. With a longer exposure time, this irregular intensity variation exposes the photochromes enough at certain locations to develop away the photoresist, resulting in a non-uniform image profile. This effect is not visible as the exposure dose is lowered.
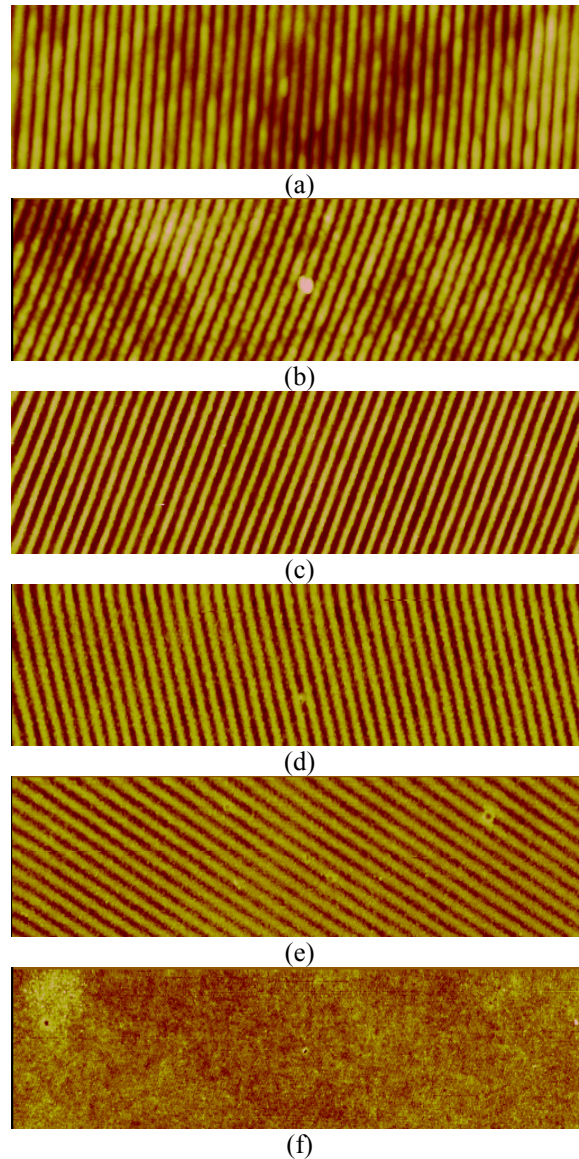

Figure 6. Additive noise with longer exposure times when imaging with SILMIL. All images are 55.5 nm half-pitch ($\lambda/7.3$) or *NA* = 1.824 at λ = 405 nm with different pseudo-dosages (PD): (a) PD = 15.3, (b) PD = 10, (c) PD = 6, (d) PD = 3, (e) PD = 2, (f) PD = 1.
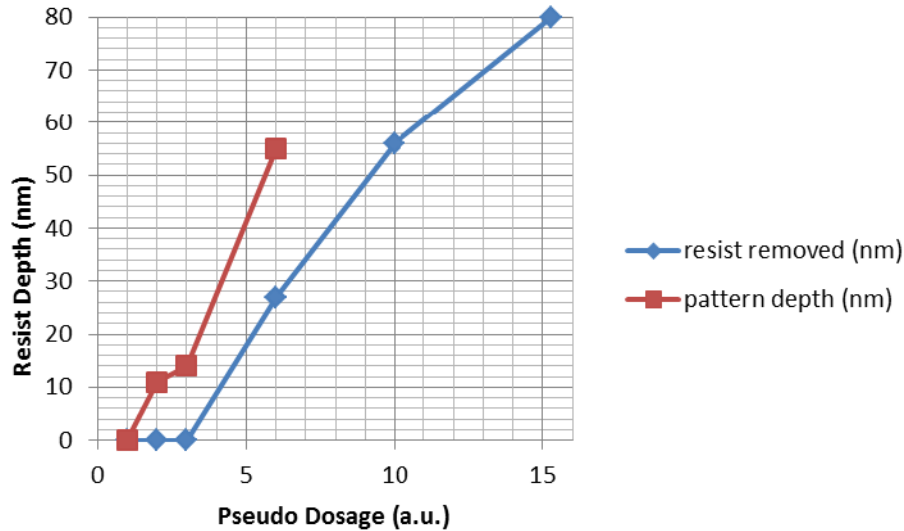
Figure 7. Summary of Fig. 6 parts (a) to (f) showing the depth of the grating patterned into the resist (square markers) as well as the amount of resist removed (measured at the peaks in the grating pattern) compared to nearby unexposed areas.

3. RESONANT ENHANCEMENT OF EVANESCENT IMAGES

The previous section outlined the design and use of our SILMIL test-bed when operating at *NA*s much higher than the refractive index of the photoresist. The obvious problem with an evanescent image is its decay into the photoresist that prevents proper pattern transfer, rendering the solid-immersion lithography setup of little commercial use at such high-*NA*s.

With this in mind, Blaikie *et al.*[35] first suggested the use of metal underlays beneath the photoresist for evanescent wave enhancement to counter image decay. Later this was the subject of a paper by Arnold *et al.*[36] detailing among other aspects, the image contrast calculations. Mehrotra *et al.*[27] continued this work and presented the working principle behind the enhancement with a numerical example involving a fictitious metal. We present that example and briefly explain that principle here to bring the reader into the subject matter of this section.

At the interface of a dielectric such as photoresist and a metal, it is possible to excite a field enhancement using the Surface Plasmon Polariton (SPP) with the transverse magnetic (TM) polarization of light. The SPP is a surface state that carries energy away from the incident beam when the energy and momentum of the beam are matched with that of the plasmons. Plasmons are a collective excitation of the electron gas that makes up the metal and are hence involved in this field redistribution.

Analysis of Maxwell's equations at the boundary of two media results in Fresnel equations. These equations predict the occurrence of such a surface state by showing peaks in the Fresnel reflection coefficients. Consider the interface of a lossy photoresist ($\varepsilon = 2.89+0.068i$ or $n = 1.7+0.02i$) with fictitious metal ($\varepsilon = -29.8$ or $n = 5.459i$) at $\lambda = 193$ nm. Such an interface exhibits reflections much larger than unity at high-*NA*s (the non-propagating evanescent regime). The implication of this is shown in Fig. 8, where we notice that the reflection at the prism-stack interface is actually attenuated due to the high-reflectance dielectric-metal interface.
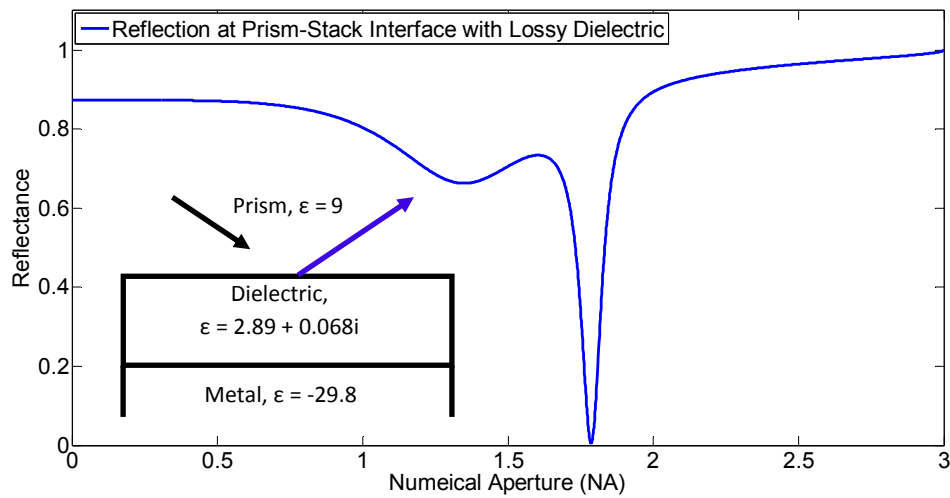
Figure 8. Attenuated Total Reflectance plot, showing reflectance vs. *NA* at the prism-stack interface with a lossy dielectric on a fictitious metal.

Figure 8 is also known as the attenuated total reflectance (ATR) plot and shows us that surface states like the SPP have the potential to extract energy away from the incident beam and redistribute the E-fields within the photoresist cavity. We have already mentioned that we wish to take advantage of this phenomenon in EIL, however the lack of metals with the required electrical permittivity prevent us from realizing this theoretical potential. In addition, we have been dealing with the TM polarization of light which is not favored by the semiconductor industry for lithography due to the resulting low contrast images. Hence, we want a similar enhancement to be possible with the TE polarization of light.

3.1 TE Polarization & Effective Gain Medium

As pointed out earlier, surface states at a two-medium interface take place when the reflection at that interface peaks to values larger than unity. Hence, upon solving the TE Fresnel reflection equation we get a very peculiar solution that requires the media under the photoresist to have negative loss, *i.e.*, exhibit gain. This is depicted in Fig. 9 (a).
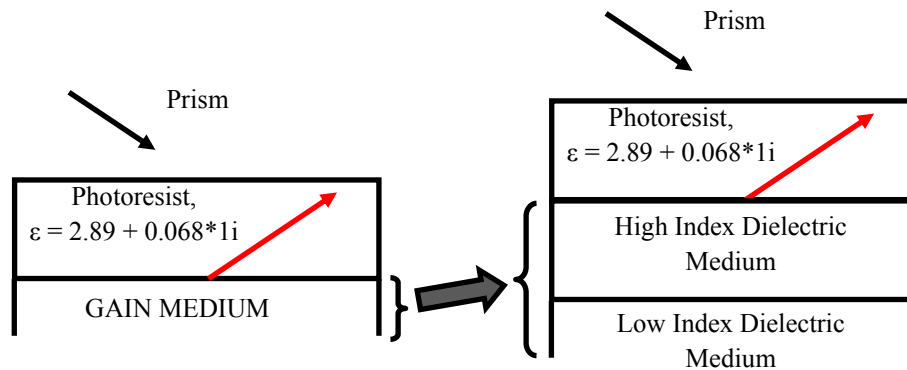

Figure 9. Gain medium underlay required for evanescent wave enhancement with TE polarization.

While this seems like a hypothetical solution, an effective gain medium (EGM) can be created simply by stacking a high index dielectric on a low index dielectric as depicted in Fig. 9 (b). The high index on low index medium stack is an EGM using effective medium theory when we concern ourselves only with the reflection at a particular *NA*.

From an intuitive perspective this is not difficult to comprehend; the high index dielectric is capable of converting an evanescent wave to a propagating state. Moreover, material choices and the thickness of the high index layer allow control over the particular wave vector that is resonated. Hence, the high index dielectric acts like a pseudo-interface to serve a similar purpose to the photoresist-metal interface considered earlier. The low-index dielectric cannot support a propagating mode of the wave causing it to be evanescent, thus serving a similar purpose to the bulk of the metal which also cannot allow a propagating wave to exist.

In fact, we are able to provide a key result that any *NA* may in fact be imaged using the above technique at an acceptable aspect ratio of 1.3 (depth/width) provided a sufficiently high index prism material is available. This may be found by using electric field intensity profiles inside the photoresist[37] and using this to compute a decay constraint which is then written in terms of the aspect ratio and *NA*. The analysis is omitted for brevity. Let us proceed to the experimental results with a system at $\lambda = 405$ nm.

Smith *et al.*[24-26] have published several papers describing the use of their solid-immersion interference lithography system (also known as the Amphibian™) to allow imaging at a *NA* as high as 1.85 at $\lambda = 193$ nm. A sapphire prism with $n = 1.92$ is used and precautions have been taken to ensure minimal effects from birefringence. We believe that the use of our method of evanescent field enhancement together with a system similar to the Amphibian™ system should allow feasible patterning of 26-nm (half-pitch) features with aspect ratios as high as 3.2. Figure 10 illustrates our design by comparing the enhancement our technique offers to conventional EIL.
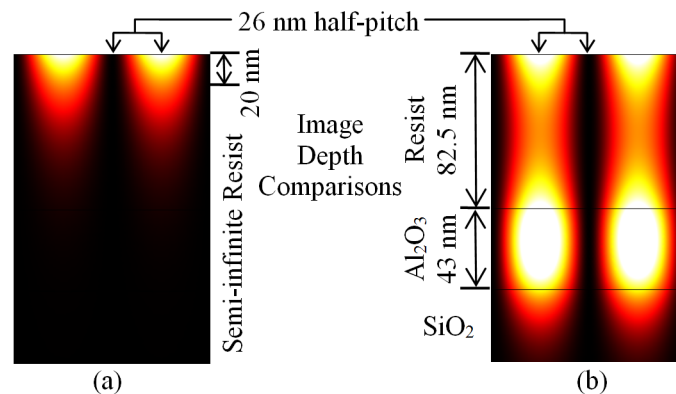

Figure 10. Imaging of 26-nm (half-pitch) evanescent features into (a) semi-infinite lossy resist giving 20-nm image depth, and (b) 82.5 nm thick lossy resist on an effective gain medium made up of 43 nm of Al$_2$O$_3$ (Sapphire) on SiO$_2$, giving an image depth of 82.5 nm.

Clearly, the proposed design fairs well in comparison to the existing technique; a fourfold increase in the image depth is visible. Here we have ensured that the image is ideally symmetric and that the minimum intensity is never below 40% of the peak intensity, a reasonable value based on experience. Note that the design in Fig. 10 has loss built into the photoresist ($n = 1.7 + 0.02i$). A 50 nm thick SiO$_2$ ($n = 1.56$) layer on any substrate should suffice as the bottom film. The refractive index of Al$_2$O$_3$ is ~2.08 as reported in Table 1. It is important to note that an Al$_2$O$_3$ thin film is the only material we know of with transparency and such a high refractive index available at $\lambda = 193$ nm. In its crystalline form (sapphire), Al$_2$O$_3$ is the prism material used to generate the evanescent wave vector in the first place. This is interesting and suggests that given a high index prism material to excite a certain *NA*, the material itself may be deposited to bring the particular wave vector into resonance.

3.2 Experiments & Results

To test out our theory with SILMIL at $\lambda = 405$ nm, we used Hafnium Oxide (HfO) as the high-index dielectric and SiO_2 as the low index dielectric. HfO has an index of refraction ~2 at $\lambda = 405$ nm, however this varies strongly with deposition parameters. AZ HiR 1075 was used as the photoresist. Through simulations, we determined the required thickness and index for each layer of the stack. The stack used consisted of a quartz coverslip ($n = 1.48$) upon which 90.3 nm of HfO was deposited. Following this, 105 nm of photoresist was spun on, followed by 15 nm of PVA. A few drops of IML were placed on top to complete the optical stack.

SILMIL was carried out on the stack described and an exposure pseudo-dose of 2.5 was used. This lies between the cases in Fig. 6 (d) and (e) with pseudo-doses of 2 & 3 respectively, that resulted in only 10-12 and 12-16 nm depths with 20 nm depth at best. Sample processing was carried out in the same manner as is detailed in section 2.4, except a development time of 4 minutes was used.

Figures 11-13 give AFM scans that show the effects of the effective gain medium surface state in enhancing the evanescent intensity profile resulting in features that are at least 4-5 times deeper than we could achieve using a pseudo-dosage of 2 in Fig. 6 (e). Note that while the pseudo-dose is similar, the effective dosage is clearly higher here because our stack now has the capability to extract a lot more energy from the incident beam than the conventional SILMIL stack did previously. We present AFM scanned profiles, cross-section areas and depth measurements for scan sizes ranging from less than 500 nm to up to 5 um. Several of these results also indicate severe resist collapse as a result of the high aspect ratios that we have achieved with evanescent interferometric lithography. This has not been previously considered possible.

We have presented scans using the 3D view feature wherever suitable. The lighting and angle is constant for all 3D views except for Fig. 14 that indicates resist collapse. The data height scale is 100 nm for all of the figures below and hence equal sized scans may be compared visually.

75 - 100 nm Depth

1 um

(a)
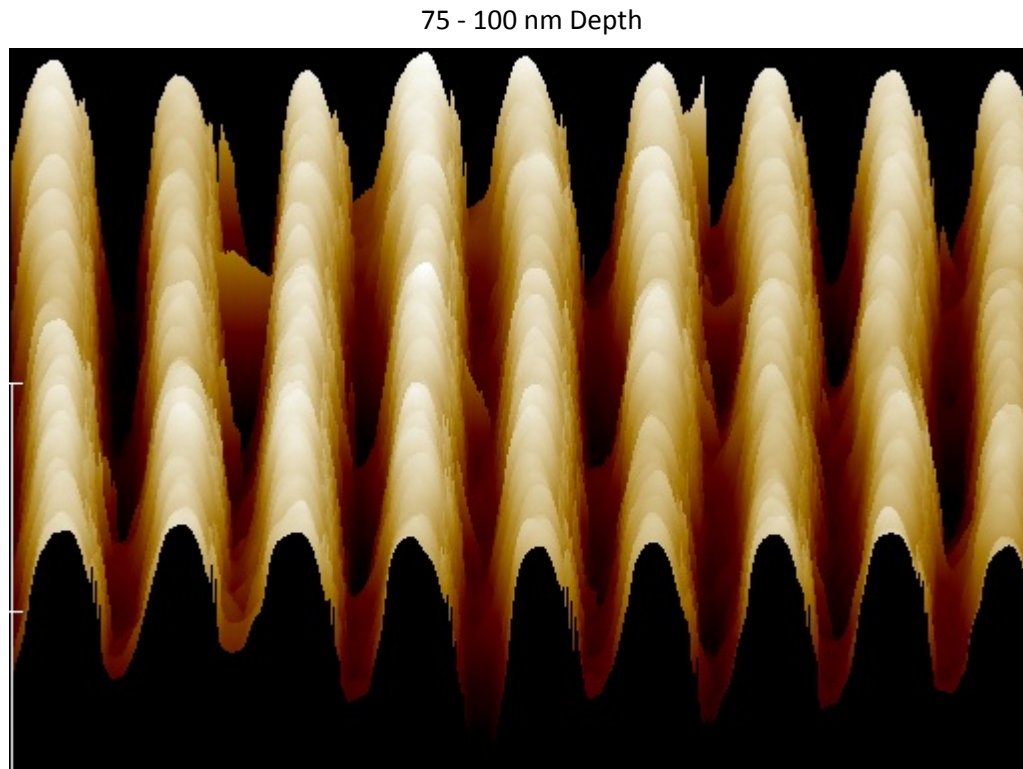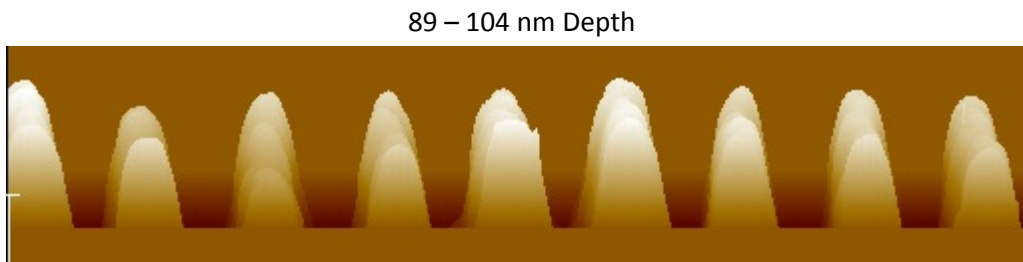
89 – 104 nm Depth

1 um

(b)

Figure 11. 1 µm scan of SILMIL at *NA* = 1.824 (55.5 nm half-pitch), λ = 405 nm and a pseudo-dose = 2.5, using an Effective Gain Medium underlay beneath 105 nm photoresist achieving features with (a) 75 – 100 nm depths and (b) 89 – 104 nm depths.
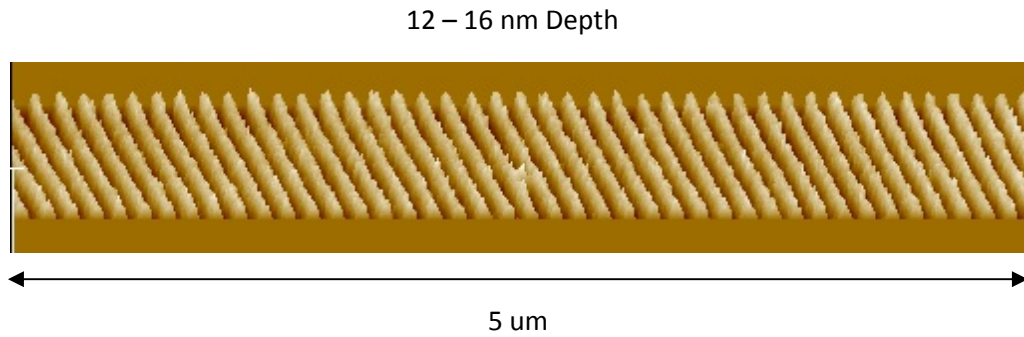
12 – 16 nm Depth

5 um

Figure 12. 5 um scan of conventional SILMIL (without the EGM), *NA* = 1.824 (55.5 nm half-pitch), λ = 405 nm (see Fig. 6), pseudo-dose = 3, giving 12-16 nm depth.

5 um
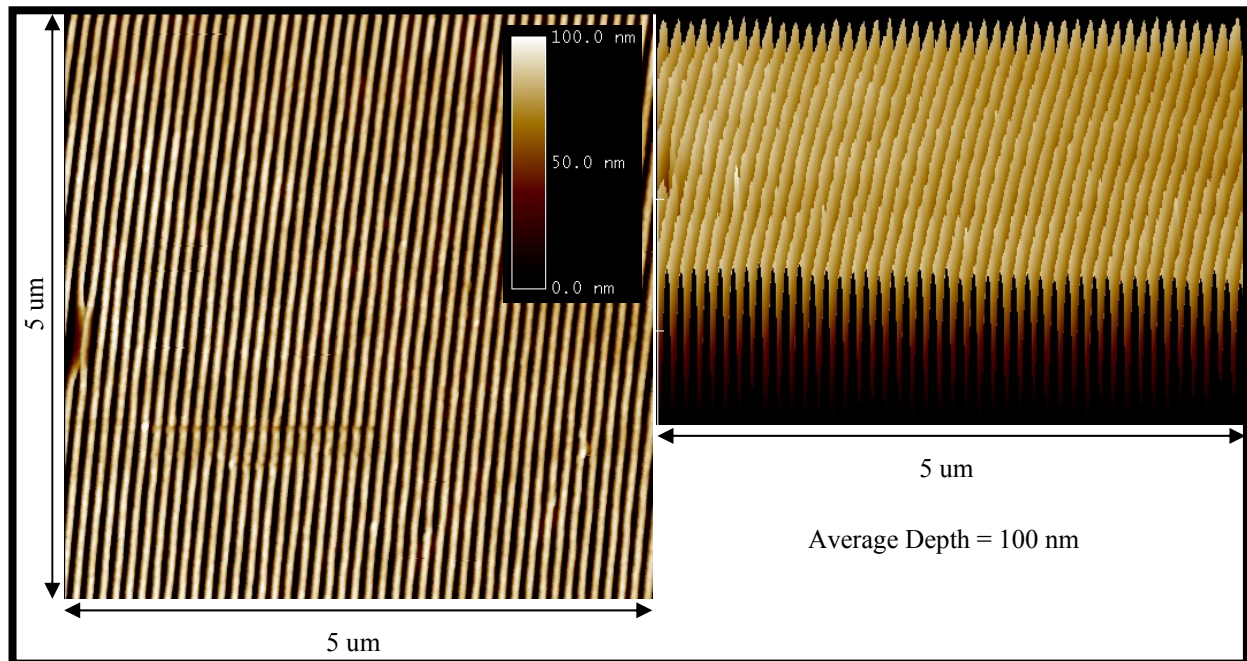
5 um

5 um

Average Depth = 100 nm

Figure 13. 5 um scan of SILMIL at *NA* = 1.824 (55.5 nm half-pitch), λ = 405 nm and a pseudo-dose = 2.5, using an Effective Gain Medium underlay in 105 nm photoresist achieving uniform features with 100 nm depth.
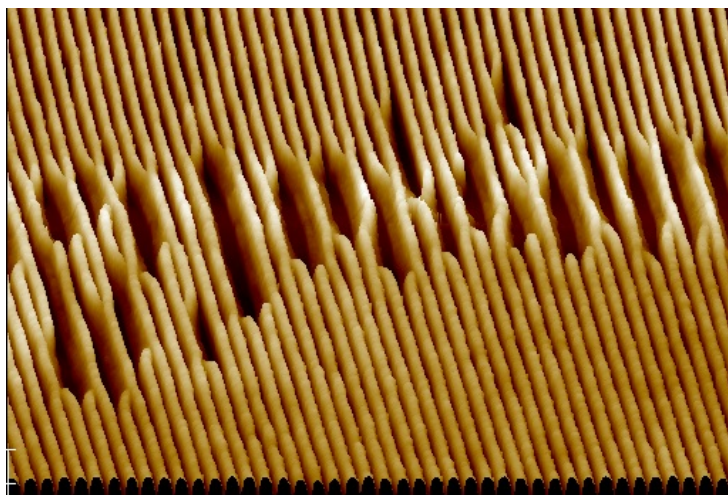
Figure 14. 5 µm scan of SILMIL at *NA* = 1.824 (55.5 nm half-pitch), λ = 405 nm using an Effective Gain Medium underlay showing resist collapse.

4. CONCLUSION

We have presented instructions regarding the setup and use of a simple solid immersion Lloyd's mirror interference lithography system to allow imaging of features at ultra-high *NA*s. We then presented intuitive insight on a newly developed theory that uses enhancement from surface states on effective gain medium underlays beneath the photoresist to enhance and redistribute evanescent interferometric images inside the photoresist cavity. We also presented a real world design at the industry standard λ = 193 nm to allow patterning of 26 nm (half-pitch) features with 82 nm depth, *i.e*., an aspect ratio of 3.2. Previously only a 20 nm depth was realizable without the use of our proposed effective gain medium made up of a layer of Al_2O_3 on SiO_2. We believe that the use of our method together with a tool such as the Amphibian[TM] should make this design feasible. Finally, we demonstrate proof of concept results at λ = 405 nm, by patterning 55.5 nm half-pitch features into 100 nm photoresist using a layer of HfO on SiO_2, *i.e*., at an aspect ratio of 1.8. Without the use of this underlay, the depth achieved under all other conditions was only 12-16 nm and 20 nm at best. We also demonstrate resist collapse due to the high aspect ratios of structures; this has not previously been considered possible. For these reasons, we believe our technique has the potential to fuel further research in solid-immersion materials and paves the way for feasible ultra-high *NA* patterning.

5. ACKNOWLEDGEMENTS

6. REFERENCES

1. R. Menon and H. I. Smith, *Journal of the Optical Society of America a-Optics Image Science and Vision*, 2006, **23**, 2290-2294.
2. R. Menon, H. Y. Tsai and S. W. Thomas, *Physical Review Letters*, 2007, **98**.
3. H. Y. S. Tsai, G. M. Wallraff and R. Menon, *Applied Physics Letters*, 2007, **91**.
4. H. Y. S. Tsai, ed., *Masters Thesis - Absorbance Modulation Optical Lithography*, Massachusetts Institute of Technology, Cambridge, MA, 2007.
5. T. L. Andrew, H. Y. Tsai and R. Menon, *Science*, 2009, **324**, 917-921.
6. J. E. Foulkes and R. J. Blaikie, *Journal of Vacuum Science & Technology B*, 2009, **27**, 2941-2946.
7. C. W. Holzwarth, J. E. Foulkes and R. J. Blaikie, *Optics Express*, 2011, **19**, 17790-17798.
8. T. Grotjohann, I. Testa, M. Leutenegger, H. Bock, N. T. Urban, F. Lavoie-Cardinal, K. I. Willig, C. Eggeling, S. Jakobs and S. W. Hell, *Nature*, 2011, **478**, 204-208.
9. E. Rittweger, K. Y. Han, S. E. Irvine, C. Eggeling and S. W. Hell, *Nature Photonics*, 2009, **3**, 144-147.
10. J. B. Pendry, *Physical Review Letters*, 2000, **85**, 3966-3969.
11. N. Fang, H. Lee, C. Sun and X. Zhang, *Science*, 2005, **308**, 534-537.
12. D. O. S. Melville and R. J. Blaikie, *Journal of Vacuum Science & Technology B*, 2004, **22**, 3470-3474.
13. M. J. Wieland, H. Derks, H. Gupta, T. van de Peut, F. M. Postma, A. H. V. van Veen and Y. Zhang, in *Alternative Lithographic Technologies II*, ed. D. J. C. Herr, 2010, vol. 7637.
14. M. J. Wieland, G. de Boer, G. F. ten Berge, M. van Kervinck, R. Jager, J. J. M. Peijster, E. Slot, S. Steenbrink, T. F. Teepen and B. J. Kampherbeek, in *Alternative Lithographic Technologies II*, ed. D. J. C. Herr, 2010, vol. 7637.
15. C. van den Berg, G. de Boer, S. Boschker, E. A. Hakkennes, G. Holgate, M. Hoving, R. Jager, J. J. Koning, V. Kuiper, Y. Ma, I. L. van Mil, H. W. Mook, T. Ooms, T. van de Peut, S. Postma, M. Sanderse, P. Scheffers, E. Slot, A. Tudorie, A. M. C. Valkering, N. Venema, N. Vergeer, A. Wiersma, S. Woutersen, M. J. Wieland and B. J. Kampherbeek, in *Alternative Lithographic Technologies III*, ed. D. J. C. Herr, 2011, vol. 7970.
16. L. Pain, B. Icard, M. Martin, C. Constancias, S. Tedesco, P. Wiedeman, A. Farah, B. J. Kampherbeek, C. Pieczulewski and H. Kandrashov, in *Alternative Lithographic Technologies III*, ed. D. J. C. Herr, 2011, vol. 7970.
17. P. Kruit, *Microelectronic Engineering*, 2007, **84**, 1027-1032.
18. B. J. Kampherbeek, M. J. Wieland, A. van Zuuk and P. Kruit, *Microelectronic Engineering*, 2000, **53**, 279-282.
19. J. E. Poelma and C. J. Hawker, *Nature Nanotechnology*, 2010, **5**, 243-244.
20. M. P. Stoykovich, H. Kang, K. C. Daoulas, G. Liu, C. C. Liu, J. J. de Pablo, M. Mueller and P. F. Nealey, *ACS Nano*, 2007, **1**, 168-175.
21. H. Arora, P. Du, K. W. Tan, J. K. Hyun, J. Grazul, H. L. Xin, D. A. Muller, M. O. Thompson and U. Wiesner, *Science*, 2010, **330**, 214-219.
22. S. M. Park, X. G. Liang, B. D. Harteneck, T. E. Pick, N. Hiroshiba, Y. Wu, B. A. Helms and D. L. Olynick, *ACS Nano*, 2011, **5**, 8523-8531.
23. J. Y. Cheng, A. M. Mayes and C. A. Ross, *Nature Materials*, 2004, **3**, 823-828.
24. B. W. Smith and J. Cashmore, in *Optical Microlithography XV*, ed. A. Yen, 2002, vol. 4691, pp. 11-24.
25. B. W. Smith, Y. F. Fan, J. M. Zhou, N. Lafferty and A. Estroff, in *Optical Microlithography XIX* ed. D. G. Flagello, 2006, vol. 6154, pp. U200-U208.
26. B. W. Smith and J. Zhou, *Proc. SPIE Optical Microlithography XX*, 2007, Vol. 6520.
27. P. Mehrotra, C. W. Holzwarth and R. J. Blaikie, *Journal of Micro/Nanolithography MEMS and MOEMS*, 2011, **10**.
28. Ondax-Incorporated, 850 E Duarte Rd Monrovia, CA, USA.
29. VLOC, VLOC Subsidary of II-VII Incorporated, New Port Richey, FL, USA.
30. Cargille, 55 Commerce Rd, Cedar Grove, NJ, USA.
31. R. Kumar, A. P. Singh, A. Kapoor and K. N. Tripathi, *Optical Engineering*, 2004, **43**, 2134-2142.
32. AZ-Electronic-Materials, Rheingaustrasse 190-196, D-65203 Wiesbaden, Germany.
33. E. D. Palik, *Handbook of Optical Constants of Solids*, Academic Press, Orlando, Florida, USA, 1985.
34. S. Z. Shang, J. D. Shao, C. Y. Liao, K. Yi, Z. X. Fan and L. Chen, *Applied Surface Science*, 2005, **249**, 157-161.
35. R. J. Blaikie, M. M. Alkaisi, S. J. McNab and D. O. S. Melville, *International Journal of Nanoscience*, 2004, **3**, 405-417.
36. M. D. Arnold and R. J. Blaikie, *Optics Express*, 2007, **15**, 11542-11552.
37. C. A. Mack, <u>Fundamental principles of optical lithography: the science of microfabrication</u>, Wiley, 2007.